# Bayesian Sensor Calibration of a CMOS-Integrated Hall Sensor Against Thermomechanical Cross-Sensitivities

Moritz Berger, *Member, IEEE*, Christian Schott, *Member, IEEE*, and Oliver Paul, *Senior Member, IEEE*

Abstract—**For the first time, Bayesian sensor calibration is used to identify efficient calibration procedures for a sensor cross-sensitive to two parasitic influences. The object under study is a thermomechanically cross-sensitive sensor system for determining the magnetic induction *B*. The packaged system comprises a Hall sensor, a stress sensor, and a temperature sensor. The three sensor signals are combined in a polynomial sensor response model with 11 parameters to determine *B* compensated for offset and cross-sensitivities. For the calibration, sensors are exposed to mechanical stress values between 0 and −68 MPa, temperatures between −40 and 100 °C, and *B* values between −25 and 25 mT. A sample of 35 sensors serves to extract the prior model parameter distribution of their fabrication run. The Bayesian experimental design is applied to identify sets of 2–8 optimal calibration conditions under I-optimality and G-optimality. The Bayesian inference then allows to obtain the posterior model parameter distribution of any uncalibrated sensor from the same run. Any such sensor is thereby turned into a *B* measuring device with individually quantified accuracy. The method was successfully applied to 15 validation sensors. In the case of I-optimality, the median root-mean-square (rms) σ values of the ±1σ confidence intervals for the extracted *B* values were found to be 113–71 μT after near-I-optimal calibrations based on 2–8 measurements. Over the entire range of temperature and mechanical stress and for applied |*B*| ≤ 25 mT, corresponding experimentally determined medians of the rms deviations between predicted and applied *B* values were found to be 89–71 μT. Analogous observations apply to G-optimality. In short, Bayesian calibration made it possible to obtain functional *B* sensors of known accuracy with significantly fewer calibration measurements than model parameters. This was enabled by prior knowledge collected by the thorough characterization of 35 prior-generating specimens.**

Index Terms—**Bayesian inference, calibration, compensation, experimental design, Hall sensor, multiple cross-sensitivities, multisensor system.**
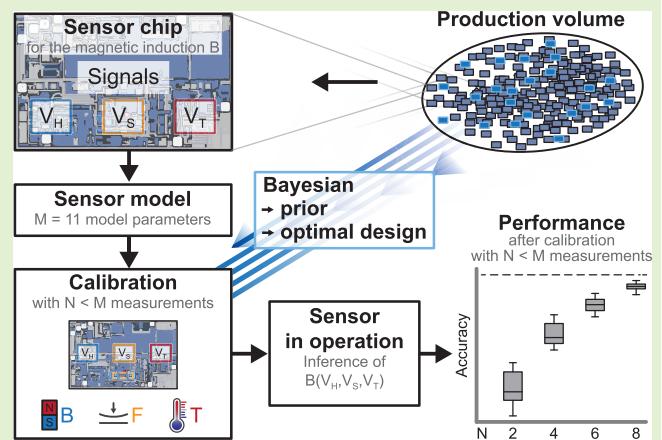
I. INTRODUCTION

UNWANTED, yet often unavoidable parasitic influences affect the operation of many sensors. Uncompensated, such cross-sensitivities cause systematic errors in the values inferred from a sensor system's output signals and thus diminish its accuracy. Temperature is well known to modulate the response of virtually every sensor. It has been shown to impair

the stability of Hall sensors [1], [2], [3], [4], pressure sensors [5], [6], [7], and mechanical stress sensors [8], [9], [10]. In fact, many sensors exhibit more than one cross-sensitivity. For example, semiconductor Hall sensors are affected not only by temperature but also by mechanical stress [11]. Volatile organic compound (VOC) sensors used as air quality sensors lack selectivity to individual air compounds [12]. Electronic tongues are cross-sensitive to various components in solutions [13]. Electronic noses have exhibited similar selectivity issues, for instance in classifying water, methanol, and ethanol vapors [14]. Likewise, cross-sensitivities to other gases, such as C_2H_5OH, SO_2, and NO, have been suspected for an ozone–humidity–temperature sensor system with a sensitive WO_3 film [15], as found in [16] for NO_2 sensors relying on this sensitive material. Among devices for physical measurands, mechanical sensors often possess cross-sensitivities to other mechanical constraints. A six-degree-of-freedom force-

moment transducer for example has exhibited for each load component cross-sensitivities to the other five components in addition to temperature [17], [18], [19]. Similarly, inertial sensors, such as gyroscopes, require compensations against stress, temperature, and the quadrature error [20], [21], [22]. All these examples highlight the importance of calibration for guaranteeing the cross-sensitivity-free and, thus, accurate operation of sensor systems.

When calibrating sensors, well-chosen calibration conditions are applied to each individual device. The outcome of the measurements performed under these conditions allows to model the individual relationship between measurand and output signals. Understandably, it is of interest to keep the number of calibration conditions low [23], [24]. This is particularly true in the context of large production volumes, where calibration is known to be time-consuming and greedy of resources [25], [26], [27], [28], [29], causing up to 50% of overall sensor costs [29]. However, a minimized calibration procedure jeopardizes one's ability to guarantee a specified high sensor accuracy.

The present study takes up the challenge of calibrating a sensor system possessing two cross-sensitivities by applying the method of Bayesian sensor calibration [4]. This method was formulated in [4] in general terms and demonstrated on a simple model case with a single, thermal cross-sensitivity. Here, the demonstration of its usefulness is therefore expanded to a more demanding case. The object under study is a Hall–stress–temperature sensor system sensitive to thermal drift and mechanical loads, fabricated in complementary metal–oxide–semiconductor (CMOS) technology. Sensor elements for the magnetic field, temperature, and mechanical stress are cointegrated with elaborate analog-to-digital circuitry [30].

Without any doubt, CMOS Hall sensors have already reached a high level of development. The 1-D Hall sensors allow to measure the out-of-plane [11] or an in-plane component of the magnetic induction B [11], [31], [32], [33], [34], [35]. The 2-D Hall sensors serve to determine angular information by measuring the in-plane components of B [34], [36], while 3-D Hall sensors give access to all three components. Such 3-D Hall sensors have, for example, combined vertical and horizontal Hall plates [37], [38] and were realized as isotropic monolithic devices [39], [40].

Nevertheless, as understandable from semiconductor transport theory, such B sensors are affected by temperature variations and mechanical stress. Temperature T acts via the temperature-dependent Hall mobility of the charge carriers [11], [41]. The cross-sensitivity to mechanical stress has its origin in piezoresistance and the piezo-Hall effect [11], [42], [43], [44]. In the former, pseudo-Hall signals are caused by shear components of the mechanical stress tensor. In the latter, the magnetic sensitivity of planar Hall plates is affected, e.g., by the sum $s = \sigma_{xx} + \sigma_{yy}$ of the in-plane normal components σ_{xx} and σ_{yy} of the mechanical stress tensor [45], [46]. Mechanical stresses responsible for both effects are caused by thermomechanical properties of the heterogeneous sensor assemblies [47], [48], [49], [50], [51] and by the swelling of the packaging materials when exposed to moisture [52], [53], [54].

Several approaches have aimed to cure these disturbances at the levels of device operation and system architecture. Integration of temperature sensors has allowed to effectively compensate thermal output signal drifts [2], [54]. The current spinning technique allows to obtain an averaged output signal largely cleared of contributions caused by the shear piezoresistance effect [55], [56], [57], [58], [59], [60], [61]. The cointegration of temperature and stress sensors together with a Hall sensor has enabled the analog compensation of the cross-sensitivities [3], [62], [63]. Alternatively, the digital signal processing of the sensor signals has also allowed to obtain Hall sensor signals largely cleared of the parasitic contributions [3], [45], [54], [64], [65]. As stated in [45], accuracies better than 1% for the temperature range required by automotive applications can be achieved only by compensating the long-term drift of the Hall sensitivity associated with mechanical stress. It is noteworthy, however, that questions concerning the efficiency of the required calibration procedures and their relation to the predictive accuracy of the compensated sensors were systematically addressed in none of these previous studies.

On a different track, data science concepts, such as machine learning (ML), have recently gained popularity in the field of sensor calibration. Therefore, they give reason to hope that the open questions may be addressed by numerically based methods. Among the most widespread ML methods in sensor calibration are artificial neural networks (ANNs) in the form of multilayer perceptrons (MLPs) [66], [67], [68], convolutional neural networks (CNNs) [69], [70], and fuzzy neural networks (FNNs) [71]. Other approaches have relied on random forests (RFs) [67], [72], [73], Gaussian process regression (GPR) [73], [74], [75], and Bayesian neural networks [76]. These methods have been applied for temperature compensation [66], [67], temporal drift compensation of field-effect transistor sensors [70], and compensating commercial water quality sensors in order to extend the calibration lifetime [69]. ANNs are much appreciated for their effectiveness in classification tasks [77], [78], [79]. An advantage of ML approaches is their ability to handle unknown, potentially complex input–output relations. This often comes at the cost of an intense training effort and the need to determine the predictive accuracy by additional validation data [66], [67], [71] or by cumbersome numerical sampling [76].

Since in the present case, the relationship between the three input quantities (B, s, T) of the sensor system under study and its three output signals is well described by low-order polynomials [80], we opt for the Bayesian approach that has already proven effective in cases with a single, thermal cross-sensitivity [4], [6]. In [4], a Hall-temperature sensor system was calibrated for the range between -30 and 150 °C. This was accomplished by applying between one and three thermal calibration conditions, implying fewer measurements than the seven parameters contained in the sensor model. The root-mean-square (rms) accuracies after these modest calibration procedures were 78, 41, and 34 μT.

The prerequisite for the effectivity of the method was the availability of prior information gained from a set of thoroughly characterized sensors termed prior-generating

specimens. The prior information is obtained by thoroughly characterizing those specimens. From their estimated sensor model parameters, one infers the sensor model parameter distribution of the ensemble in the form of a prior mean and a prior covariance matrix. This prior information is combined with the limited evidence provided by the calibration of other sensors about their individual responses. Updated model parameters and an updated covariance matrix of each individual sensor are thereby obtained.

Section II recalls the central mathematical elements of Bayesian sensor calibration. In Section III, we describe the mentioned Hall–stress–temperature multisensor system and the experimental infrastructure and procedures to calibrate it. The results in Section IV demonstrate that these sensors can be effectively compensated against mechanical stress and temperature variations with five or fewer thermomechanical calibration conditions while offering a high sensor accuracy. Then, Section V discusses the results and is followed by the conclusions.

II. BAYESIAN CALIBRATION

Since this work applies the method described in detail in [4], here, we only summarize the most important definitions and results.

We use the term sensor system as a synonym for the CMOS-integrated, packaged Hall–stress–temperature sensor system providing the application and test case of this article. An individual sensor system is considered as a *specimen* of a *sensor ensemble* with statistically distributed properties. A specimen or a group of specimens, therefore, constitute samples of the ensemble. We reserve bold symbols for vectors and matrices and roman symbols for scalar values.

In the present case, the magnetic induction B is the measurand of interest. It plays the role of the dependent variable. The output signals of the Hall sensor and the stress and temperature sensing elements of the sensor system are summarized as $\boldsymbol{v} = (V_H, V_S, V_T)$. The components of $\boldsymbol{v}$ provide the independent variables of the Bayesian analysis. The $\boldsymbol{v}$-dependent measurand B is modeled by $\boldsymbol{\phi}(\boldsymbol{v})^\top \boldsymbol{w}$ using a set of basis functions $\boldsymbol{\phi}(\boldsymbol{v})^\top = (\phi_1(\boldsymbol{v}), \ldots, \phi_M(\boldsymbol{v}))$ and the corresponding model parameters $\boldsymbol{w} = (w_1, \ldots, w_M)^\top$, where $(\cdot)^\top$ denotes the matrix transposition and M is the model dimension. In the present case, $M = 11$. The goal of optimal calibration is to find $\boldsymbol{w}$ such that B can be inferred from $\boldsymbol{v}$ with the highest possible accuracy. A crucial role in this process is played by the design matrix $\boldsymbol{\Phi}(\boldsymbol{V})$ defined as [77, Ch. 3]

$$\boldsymbol{\Phi}(\boldsymbol{V}) = \begin{pmatrix} \phi_1(\boldsymbol{v}_1) & \cdots & \phi_M(\boldsymbol{v}_1) \\ \vdots & \ddots & \vdots \\ \phi_1(\boldsymbol{v}_N) & \cdots & \phi_M(\boldsymbol{v}_N) \end{pmatrix} \tag{1}$$

for any list $\boldsymbol{V} = (\boldsymbol{v}_1, \ldots, \boldsymbol{v}_N)$ of N sensor output signal vectors.

The Bayesian sensor calibration method consists of three steps.

1) Prior information about the sensor parameter vectors $\boldsymbol{w}$ of a considered ensemble is gathered by thoroughly characterizing a group of Q so-called prior-generating specimens, which constitute a sample of the ensemble. In the present case, $Q = 35$. Therefore, the so-called prior probability distribution $p_0(\boldsymbol{w})$ is constructed.

2) The second step consists of two substeps, namely, a Bayesian update and a Bayesian design of experiment.

   a) The Bayesian update considers exposing any previously uncalibrated specimen to a small set of N calibration conditions, whereby its output signals $\boldsymbol{V}$ and the corresponding applied magnetic induction values $\boldsymbol{B} = (B_1, \ldots, B_N)^\top$ are collected. From $p_0(\boldsymbol{w})$, $\boldsymbol{V}$, and $\boldsymbol{B}$, one obtains the updated probability distribution $p_1(\boldsymbol{w})$. This allows to turn the previously uncalibrated specimen into a measuring device allowing to translate any combination of its output signals $\boldsymbol{v}$ into a prediction of the applied B. This inference is achieved by the posterior predictive response $B_1(\boldsymbol{v}, \boldsymbol{V}, \boldsymbol{B})$ and its accuracy expressed by the posterior predictive variance $\sigma_1^2(\boldsymbol{v}, \boldsymbol{V})$.

   b) The Bayesian design of experiment then aims for optimizing the postcalibration measurement accuracy of previously uncalibrated specimens. It minimizes $\sigma_1^2(\boldsymbol{v}, \boldsymbol{V})$ subject to a criterion of one's choice. For this purpose, a numerical search within the range Ω of output signals arising from the range of expected operating conditions of the specimen is carried out. As a result, one identifies the combination of sensor output signals $\boldsymbol{V}_{\min}$ achieving minimality.

3) In the third step, previously uncalibrated specimens of the ensemble are calibrated. Any such device is thereby exposed to calibration conditions that are known to produce sensor outputs $\boldsymbol{V}_{\mathrm{cal}}$ near $\boldsymbol{V}_{\min}$. Based on its individual calibration results, $\boldsymbol{V}_{\mathrm{cal}}$, the specimen is turned into a measuring device whose output signals $\boldsymbol{v}$ allow to infer B. This inference uses the posterior predictive response $B_1(\boldsymbol{v}, \boldsymbol{V}_{\mathrm{cal}}, \boldsymbol{B})$, while the accuracy of the inference is quantified by $\sigma_1^2(\boldsymbol{v}, \boldsymbol{V}_{\mathrm{cal}})$.

These steps are now presented in the mathematical detail required by the experimental study in Sections III and IV. First, for prior generation, each prior-generating specimen is exposed to 1110 characterization conditions. For each specimen numbered $i = 1, \ldots, Q$, one thereby records sensor output signals $\boldsymbol{V}_i = (\boldsymbol{v}_{i1}, \ldots, \boldsymbol{v}_{i1110})$. The B values applied during characterization are listed in the column vector $\boldsymbol{B} = (B_1, \ldots, B_{1110})^\top$.

Using standard linear regression, the model parameter vector $\boldsymbol{w}_i$ of prior-generating specimen no. i is then obtained by

$$\boldsymbol{w}_i = \left\{ \boldsymbol{\Phi}(\boldsymbol{V}_i)^\top \boldsymbol{\Phi}(\boldsymbol{V}_i) \right\}^{-1} \boldsymbol{\Phi}(\boldsymbol{V}_i)^\top \boldsymbol{B} \tag{2}$$

where the term in front of $\boldsymbol{B}$ denotes the well-known Moore–Penrose pseudoinverse [81] of the design matrix evaluated at $\boldsymbol{V}_i$. From the distribution of $\boldsymbol{w}_i$ in $\boldsymbol{w}$ space, one derives the prior probability distribution $p_0(\boldsymbol{w})$ of the ensemble and approximates it by a multivariate normal distribution with

mean

$$\boldsymbol{w}_0 = \frac{1}{Q}(\boldsymbol{w}_1 + \cdots + \boldsymbol{w}_Q) \tag{3}$$

and covariance matrix

$$\boldsymbol{\Sigma}_0 = \frac{Q+1}{Q(Q-M-2)}\Delta \boldsymbol{W}^\top \Delta \boldsymbol{W} \tag{4}$$

where $\Delta \boldsymbol{W} = (\boldsymbol{w}_1 - \boldsymbol{w}_0, \ldots, \boldsymbol{w}_Q - \boldsymbol{w}_0)^\top$ lists the mean-centered $\boldsymbol{w}_i$ vectors. With $\boldsymbol{w}_0$ and $\boldsymbol{\Sigma}_0$, one is able to infer B from an output signal $\boldsymbol{v}$ of any uncalibrated specimen of the ensemble. This B value is given by

$$B_0(\boldsymbol{v}) = \boldsymbol{\phi}(\boldsymbol{v})^\top \boldsymbol{w}_0 \tag{5}$$

while the accuracy of the prediction is quantified by the variance

$$\sigma_0^2(\boldsymbol{v}) = \sigma^2 + \boldsymbol{\phi}(\boldsymbol{v})^\top \boldsymbol{\Sigma}_0 \boldsymbol{\phi}(\boldsymbol{v}) \tag{6}$$

where σ^2 denotes the variance of the individual B measurement of thoroughly characterized specimens. The quantities $B_0(\boldsymbol{v})$ and $\sigma_0^2(\boldsymbol{v})$ are the mean and variance of the distribution of B values inferrable from output signals $\boldsymbol{v}$ of any uncalibrated specimen, given only the prior information. The prior predictive probability distribution of B is in fact the normal distribution defined by these parameters. This is a consequence of the assumed multivariate normality of $p_0(\boldsymbol{w})$ and of the Gaussian statistics of the individual measurement.

When evidence about a specimen's individual response becomes available in the form of calibration data $\boldsymbol{V} = (\boldsymbol{v}_1, \ldots, \boldsymbol{v}_N)$ and $\boldsymbol{B} = (B_1, \ldots, B_N)^\top$, Bayes' theorem allows to determine the posterior probability distribution $p_1(\boldsymbol{w})$ valid for the specimen. This is again a multivariate normal distribution, with posterior mean [77, Sec. 3.3.1]

$$\boldsymbol{w}_1(\boldsymbol{V}, \boldsymbol{B}) = \boldsymbol{\Sigma}_1(\boldsymbol{V})\left(\boldsymbol{\Sigma}_0^{-1}\boldsymbol{w}_0 + \frac{1}{\sigma^2}\boldsymbol{\Phi}(\boldsymbol{V})^\top \boldsymbol{B}\right) \tag{7}$$

and posterior covariance matrix

$$\boldsymbol{\Sigma}_1(\boldsymbol{V}) = \left(\boldsymbol{\Sigma}_0^{-1} + \frac{1}{\sigma^2}\boldsymbol{\Phi}(\boldsymbol{V})^\top \boldsymbol{\Phi}(\boldsymbol{V})\right)^{-1}. \tag{8}$$

Equations (7) and (8) describe the Bayesian updates of $\boldsymbol{w}_0$ and $\boldsymbol{\Sigma}_0$ mediated by the new evidence $\boldsymbol{V}$ and $\boldsymbol{B}$ complementing the evidence available from the prior characterization.

Similar to the prior case, $\boldsymbol{w}_1(\boldsymbol{V}, \boldsymbol{B})$ and $\boldsymbol{\Sigma}_1(\boldsymbol{V})$ enable B to be inferred from output signals $\boldsymbol{v}$ of the specimen that has yielded $(\boldsymbol{V}, \boldsymbol{B})$ during calibration. This posterior predictive value is

$$B_1(\boldsymbol{v}, \boldsymbol{V}, \boldsymbol{B}) = \boldsymbol{\phi}(\boldsymbol{v})^\top \boldsymbol{w}_1(\boldsymbol{V}, \boldsymbol{B}) \tag{9}$$

and the corresponding posterior predictive variance is

$$\sigma_1^2(\boldsymbol{v}, \boldsymbol{V}) = \sigma^2 + \boldsymbol{\phi}(\boldsymbol{v})^\top \boldsymbol{\Sigma}_1(\boldsymbol{V})\boldsymbol{\phi}(\boldsymbol{v}). \tag{10}$$

The 68.3% confidence interval of the posterior prediction is the $\pm\sigma_1(\boldsymbol{v}, \boldsymbol{V})$ range surrounding $B_1(\boldsymbol{v}, \boldsymbol{V}, \boldsymbol{B})$.

For the design of experiment, as in [4], we consider two optimization criteria, namely, G-optimality and I-optimality.

The G-optimality criterion [82] considers the objective function

$$f_G(\boldsymbol{V}) = \max_{\boldsymbol{v} \in \Omega} \sigma_1^2(\boldsymbol{v}, \boldsymbol{V}) \tag{11}$$

with optimum defined as

$$\boldsymbol{V}_{\min} = \min_{\boldsymbol{V} \in \Omega^N} f_G(\boldsymbol{V}). \tag{12}$$

In contrast, I-optimality [82], [83] relies on the objective function

$$f_I(\boldsymbol{V}) = \frac{1}{V_\Omega} \int_\Omega \sigma_1^2(\boldsymbol{v}, \boldsymbol{V}) d\boldsymbol{v} \tag{13}$$

and identifies the optimum at

$$\boldsymbol{V}_{\min} = \min_{\boldsymbol{V} \in \Omega^N} f_I(\boldsymbol{V}). \tag{14}$$

Finally, the Bayesian sensor calibration is ready to be applied to uncalibrated specimens. In this work, such uncalibrated specimens serve to experimentally demonstrate the validity of the outlined method. They are therefore termed validation specimens. Since the optimal $\boldsymbol{V}_{\min}$ lists sensor output signals rather than calibration conditions (B, s, and T), it can be challenging to perform the calibration under the optimal conditions. Nevertheless, by analyzing the responses of the prior-generating specimens, one is able to identify calibration conditions that within the group of prior-generating specimens have yield output signals close to the optimum. When these near-optimal calibration conditions are applied to a validation specimen, they produce the specimen's individual near-optimal output signals $\boldsymbol{V}_{\text{cal}}$. The specimen's individual $\boldsymbol{w}_1(\boldsymbol{V}_{\text{cal}}, \boldsymbol{B})$ and $\boldsymbol{\Sigma}_1(\boldsymbol{V}_{\text{cal}})$ is then updated from $\boldsymbol{w}_0$ and $\boldsymbol{\Sigma}_0$ according to (7) and (8), respectively. Using (9) and (10), these allow to infer B from the validation specimen's measured output signals $\boldsymbol{v}$ using the posterior predictive response $B_1(\boldsymbol{v}, \boldsymbol{V}_{\text{cal}}, \boldsymbol{B})$ with accuracy quantified by $\sigma_1(\boldsymbol{v}, \boldsymbol{V}_{\text{cal}})$.

III. EXPERIMENT

The Bayesian sensor calibration methodology is now applied to the sensor system mentioned above. Details of the system are presented in Section III-A. The experimental setup and data acquisition are then described in Sections III-B and III-C, respectively.

A. Sensor System

The Hall sensor microsystem under study was fabricated in an industrial 180-nm CMOS technology. An optical micrograph of an unpackaged sensor chip in Fig. 1 highlights the Hall sensor, the mechanical stress sensor, and the temperature sensor. The Hall sensor consists of two interconnected Hall plates sensitive to the out-of-plane magnetic induction component B and providing the Hall voltage V_H. The respective output signals V_S and V_T of the stress and temperature sensors reflect s and T near the Hall sensor. Further details about the system and its architecture are reported in [30].

The Hall voltage V_H is described by

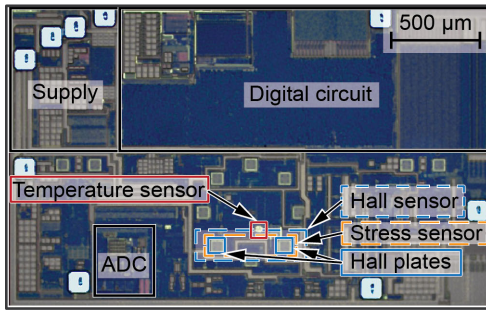$$V_H(B, s, T) = S_A(s, T)B + V_{\text{off}}(s, T) \tag{15}$$

Fig. 1. Optical micrograph of an unpackaged CMOS sensor chip comprising a pair of n-doped silicon Hall plates, a temperature sensor based on n- and p-doped resistors [2], and a piezoresistive stress sensor (orange dashed line), realized by 16 n- and p-doped resistors placed around the two Hall plates [8]. The stress sensor is electrically connected in a Wheatstone bridge configuration. Output signals are conditioned and digitized by cointegrated analog and digital circuitry [30].

where $S_A(s, T)$ and $V_{off}(s, T)$ denote the stress- and temperature-dependent absolute Hall sensitivity and the residual offset voltage at $B = 0$, respectively.

The purpose of the sensor system is to allow to infer B from the sensor signals $v = (V_H, V_S, V_T)$. By rearranging (15), this inference is achieved by

$$B(v) = \frac{V_H}{S_A(V_S, V_T)} - B_{off}(V_S, V_T) \quad (16)$$

where $1/S_A(V_S, V_T)$ and $B_{off}(V_S, V_T) = V_{off}/S_A$ denote the inverse Hall sensitivity and the equivalent offset field, respectively. Note that the arguments of S_A and B_{off} are chosen to be the sensor signals V_S and V_T reflecting the parasitic influences s and T.

The stress sensor is designed to be sensitive [8] to mechanical stress exerted on the Hall sensor, by external constraints, e.g., compressive forces F acting on the sensor package [80] in addition to thermomechanical loads [48]. Values of s caused by perpendicular forces up to 20 N are expected to be about -68 MPa at 25 °C [3], [80].

Fig. 2 shows the measured values of $1/S_A$ and B_{off} of a representative specimen as a function of V_S and V_T. The data were obtained by varying the temperature from -40 to 100 °C and applying perpendicular compressive forces F to the sensor package between 0 and 20 N, as detailed in Section III-B. The sensor signals V_H, V_S, and V_T were shifted to reduce their values at the reference conditions $B = 0$ mT, $T = 30$ °C, and $F = 0$ N to zero. In addition, they were rescaled.

Inspection of the data in Fig. 2 shows that in comparison with $F = 0$ N, the applied forces of 20 N reduce S_A by between 3.6% and 4.5%, depending on temperature. Similarly, at $F = 0$ N, S_A is reduced from the room temperature value by about 27% at 100 °C and increased by about 42.6% at -40 °C. It turns out that $1/S_A$ is well fit by a polynomial model of degree 4 in V_S and V_T, while B_{off} is well modeled by a second-degree polynomial. An appropriate polynomial model is selected in Section IV-A.

The present study covers 50 specimens assembled as pairs in 25 dual-die TSSOP-16 packages [4], [80]. The specimens are split into two groups, the first of which comprises $Q = 35$ randomly selected specimens for the generation of the prior and the remaining 15 specimens serve for validation.
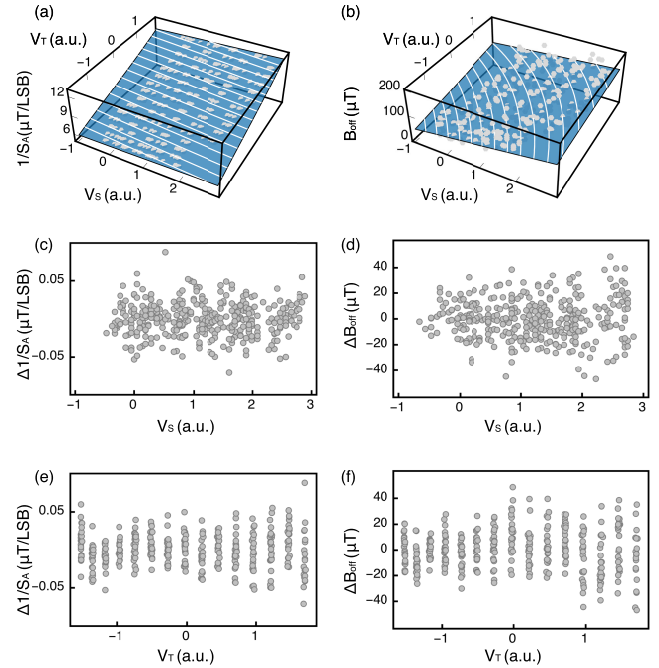

Fig. 2. (a) $1/S_A$ and (b) B_{off} of a representative specimen as a function of rescaled V_S and V_T. The blue surfaces with white level lines are the result of a polynomial fit of the data. Respective residuals, i.e., the deviations of (c) and (e) $1/S_A$ and (d) and (f) B_{off} data from their fit surfaces, projected along (c) and (d) V_S- and (e) and (f) V_T-axes.

The first group is numbered $i = 1, \ldots, 35$, while the second is assigned the numbers $i = 36, \ldots, 50$.

B. Experimental Setup

Fig. 3 shows a schematic of the experimental setup with a close-up photograph of a sensor system soldered to a printed circuit board (PCB). An air streamer (Dragon Air Streamer, Froilabo, France) connected to the thermal chamber enables to vary T of the specimen hosted by the chamber. An xyz-table allows to align the thermal chamber within a Helmholtz coil, which serves to apply B between -25 and 25 mT. The Helmholtz coil was calibrated using a Tesla meter (Gauss/Tesla Meter Series 8000, F.W. BELL, Milwaukie, OR, USA). The custom-built thermal chamber rests on a motorized test stand (Test Stand ESM303, Mark-10, Copiague, NY, USA). A movable, customized spring load system equipped with a reference force sensor (Mark-10, Series 5 Force Gauge, Copiague, NY, USA) allows to expose the specimen packages to perpendicular forces F by pushing a rod against their surface. The rod penetrates the thermal chamber through an opening in its ceiling. Under the applied forces, the output signals of the stress sensors cover a comparable range of values as when specimens are exposed to other test procedures such as high-temperature operating lifetime (HTOL) testing. The setup is controlled by a LabView routine.

C. Characterization

The 35 prior-generating specimens were exposed to the following characterization conditions:

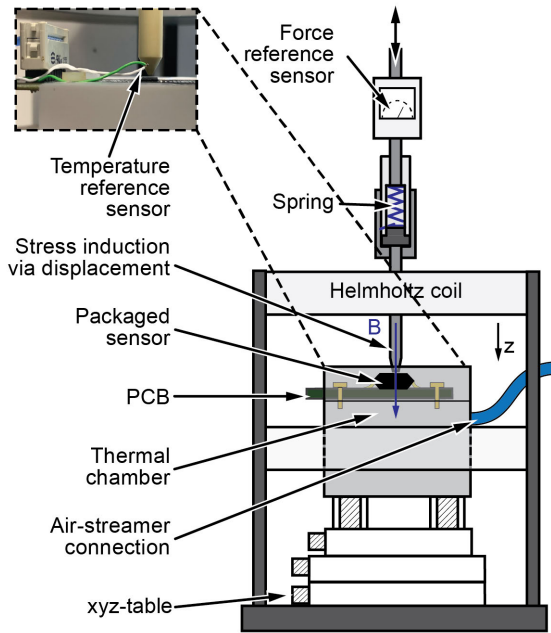1) T was varied from -40 to 100 °C in steps of nominally 10 °C;

Fig. 3. Schematic of the automated characterization setup for the magnetothermomechanical calibration of Hall sensor systems. The magnetic induction B, mechanical stress s, and temperature T are applied using a Helmholtz coil, a motorized compression test stand, and an air streamer, respectively. The photograph shows a packaged sensor soldered to a PCB with the tip of the movable rod pressed against the sensor surface as well as a temperature reference sensor.

2) At each $T < 100$ °C, F was varied from 0 to 20 N in steps of nominally 5 N, while for $T = 100$ °C, F was varied in the same steps up to 15 N;
3) At each T and F combination, B was set to -25, 0, and 25 mT;
4) At each condition, five successive readings of the three sensor signals were recorded.

Fig. 4 shows the measurement history of a representative specimen. The first three graphs show T, as measured by the temperature reference sensor, F as measured by the force reference sensor, and the applied B values. The last three graphs show the resulting output signals V_H, V_S, and V_T. Fig. 4(g) shows the range Ω in $\boldsymbol{v}$ space enveloping 97% of all 35×1110 data points of the prior-generating specimens.

For the Bayesian data analysis in Section IV, the output data of each prior-generating specimen are formatted as the list of independent variables $\boldsymbol{V}_i = (\boldsymbol{v}_{i1}, \ldots, \boldsymbol{v}_{i1110})$ with $i = 1, \ldots, 35$. The dependent variable vector of the Bayesian analysis common to all prior-generating specimens forms the column vector $\boldsymbol{B} = (B_1, \ldots, B_{1110})^\top$.

IV. RESULTS

Section IV-A is dedicated to the selection of a polynomial model able to adequately describe the observed sensor responses. Thereafter, we closely follow the procedure laid out in Section II.

A. Model Selection

It is guided by three requirements. First, the model needs to be linear in its parameters $\boldsymbol{w}$. Second, its complexity described
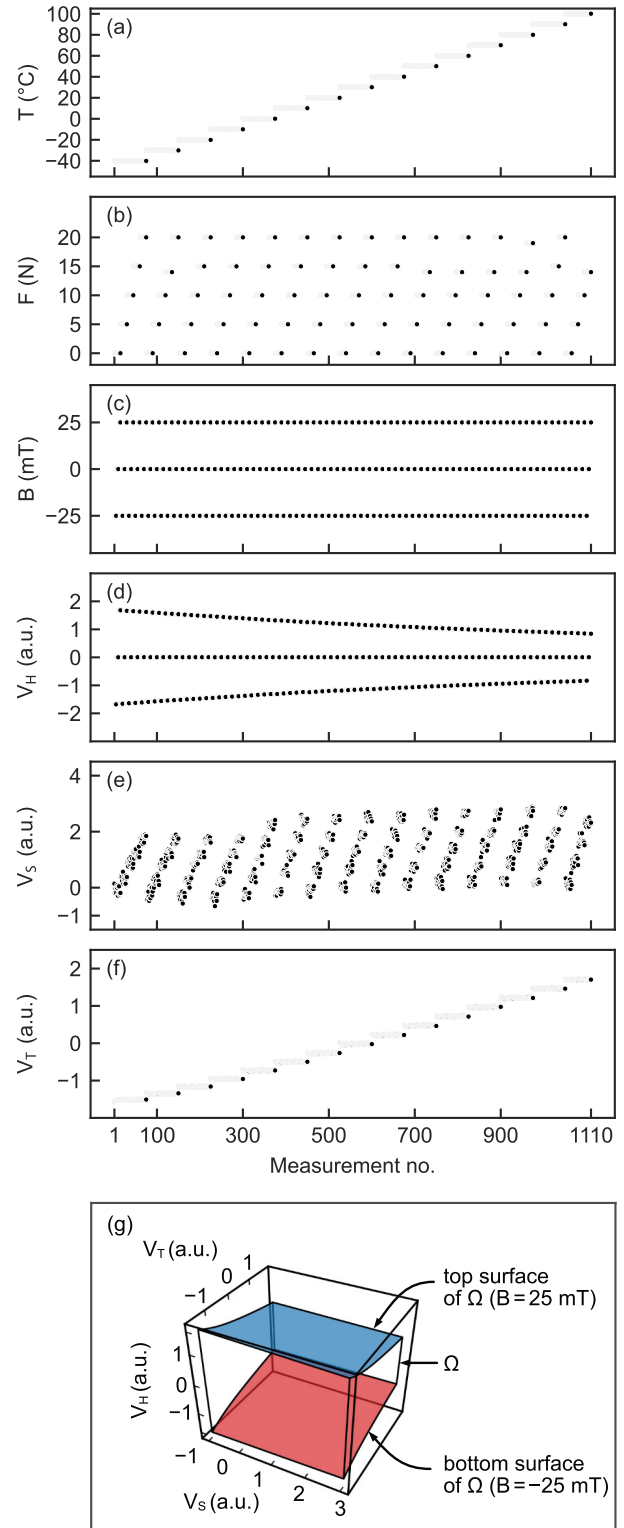

Fig. 4. Exemplary characterization history of a specimen with 1110 measurements consisting of three B values applied each at 15 nominal T values and five F values for $T < 100$ °C and four F values for $T = 100$ °C. At each condition, V_H, V_S, and V_T were recorded five times. (a) Nominal T values, (b) force values F, and (c) B values. Resulting sensor output signals (d) V_H, (e) V_S, and (f) V_T. (g) Range Ω in signal space covered by the applied characterization conditions. The top and bottom surfaces correspond to $B = \pm 25$ mT.

by M should be large enough to allow the experimental data to be accurately fit. Third, M should at the same time be as
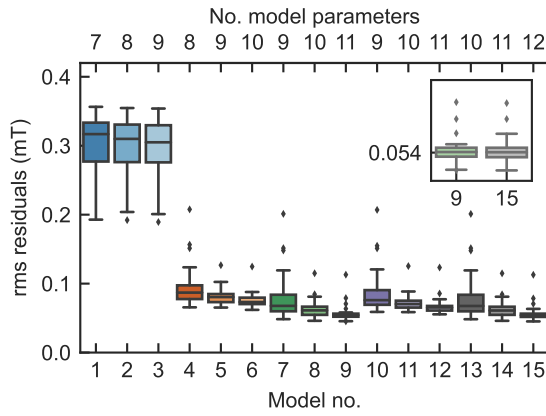
Fig. 5. Fit quality of the 15 investigated polynomial models listed in Table I in the Appendix. Each box plot captures the distribution of the 35 rms residuals ΔB_i [cf. (17)] of the fits of the prior-generating sensor data with the corresponding model by the method of least squares.

small as possible to avoid overfitting [84], [85], [86], [87]. With the expectation that response surfaces such as those in Fig. 2 lend themselves to Taylor series expansion, we focus on polynomial models in the variables V_H, V_S, and V_T of increasing complexity. A selection of 15 such models is proposed in the Appendix. For each model, we proceed as follows. For the prior-generating specimens, we carry out the linear regression of their data $\boldsymbol{V}_i$ with $i = 1, \ldots, 35$, and $\boldsymbol{B}$ according to (2) and hence obtain the list of parameter vectors $\boldsymbol{w}_i$. The rms deviation ΔB_i between the data $\boldsymbol{B}$ and the fit function of specimen no. i evaluated at $\boldsymbol{V}_i$, i.e., $\boldsymbol{\Phi}(\boldsymbol{V}_i)\boldsymbol{w}_i$, is then given by

$$\Delta B_i = \frac{1}{\sqrt{1110}} |\boldsymbol{B} - \boldsymbol{\Phi}(\boldsymbol{V}_i)\boldsymbol{w}_i| \quad (17)$$

where $|\cdot|$ denotes the Euclidean norm. The results are compiled in Fig. 5. For each model, the 35 resulting rms deviations are summarized as a box plot. The box represents the interquartile range (IQR), with the median indicated by the solid line in the box; the whiskers embrace all data points lying within 1.5 IQRs below the first quartile and above the third quartile. Values beyond the whiskers are considered as outliers and plotted as diamond symbols. Overall, models nos. 9 and 15 are found to achieve the best fits, as highlighted also by the inset in Fig. 5. Since the performance of the simpler model no. 9 with $M = 11$ equals that of model no. 15 with $M = 12$, model no. 9 is adopted for further data analysis. A formal model comparison and selection, as discussed, e.g., in [77, Sec. 3.4], [78, Ch. 5], and [88, Ch. 7], is beyond the scope of this work and delayed to a future study. In conclusion, the result of the model selection is the vector of basis functions

$$\begin{aligned}
&\boldsymbol{\phi}(\boldsymbol{v}) \\
&= \big(1, V_T, V_S, V_S V_T, \\
&\quad V_H, V_H V_T, V_H V_T^2, V_H V_T^3, V_H V_T^4, V_H V_S, V_H V_S V_T\big)^\top. \quad (18)
\end{aligned}$$

Note that the first four terms are independent of V_H and are thus well-suited for modeling B_{off}, while the other seven terms are proportional to V_H and thus aptly model V_H/S_A. The model dimension $M = 11$ sets the minimum number of

calibration conditions required to determine $\boldsymbol{w}$ of a specimen without prior knowledge. Note that in Fig. 2, the fit surface for $1/S_A$ was obtained with the last seven basis functions in (18), whereas that of B_{off} relied on the first four.

B. Prior Generation

The model parameter vectors $\boldsymbol{w}_i$ obtained with model no. 9 for the 35 prior-generating specimens constitute the database for determining $p_0(\boldsymbol{w})$ of the sensor ensemble, of which they constitute a sample. By applying (3) and (4), we compute the mean $\boldsymbol{w}_0$ and the covariance matrix $\boldsymbol{\Sigma}_0$. Fig. 6(a1) shows $\boldsymbol{\Sigma}_0$ by a heat plot.

From $\boldsymbol{w}_0$ and $\boldsymbol{\Sigma}_0$, using (5) and (6), we next infer the prior predictive mean $B_0(\boldsymbol{v})$ as a function of $\boldsymbol{v} = (V_H, V_S, V_T)$ and similarly the prior predictive standard deviation $\sigma_0(\boldsymbol{v})$. The value of σ required in (6) is taken to be 57.7 μT. This value is determined from the 35×1110 prior-generating specimen data as $\sigma = (\sum_i \Delta B_i^2 / 35)^{1/2}$. The prior predictive confidence range of the inferred $B_0(\boldsymbol{v})$ value, quantified by $\sigma_0(\boldsymbol{v})$, is plotted in Fig. 6(b1). In fact, the plot shows the values of $\sigma_0(\boldsymbol{v})$ on the top surface of Ω projected onto the (V_S, V_T)-plane. This choice is justified by the observation that, for given V_S and V_T, σ_0 assumes its maximum in the V_H-direction either at $B = 25$ mT or $B = -25$ mT, i.e., on the top or bottom surfaces of Ω in Fig. 4(g), respectively. Furthermore, the two values of σ_0 on these two surfaces differ little due to the modest Hall sensor offset. The plot also shows the (V_S, V_T) data provided by the characterization of a representative prior-generating specimen. The white dashed rectangle defines the extent of Ω in the (V_S, V_T)-plane. It embraces 97% of the characterization data acquired with the prior-generating specimens for 0 N $\le F \le 20$ N and -40 °C $\le T \le 100$ °C. It covers the ranges $-1 \le V_S \le 3$ and $-1.6 \le V_T \le 1.8$.

C. Calibration at near-optimal stress–temperature conditions

The next goal is to identify combinations of N calibration conditions such that the corresponding sensor outputs of any uncalibrated specimen minimize its posterior predictive uncertainty (σ_1^2) with respect to the chosen optimality condition. The search for optimal conditions is carried out within the domain Ω. Thereby, one ensures that the search reasonably covers the range of operating conditions to which the specimen will later be exposed and which were consequently covered during the characterization of the prior-generating specimens.

We perform the calibration measurements exclusively with $B = \pm 25$ mT. This is justified by the fact that for given (V_S, V_T), the relationship between B and V_H is highly linear and thus well determined by a pair of measurements. Moreover, these measurements should ideally lie as far apart as possible in the V_H-direction. Within the operating range, this is the case when $B = \pm 25$ mT. Therefore, the corresponding $\boldsymbol{v}$ search domain by definition consists of the top and bottom surfaces of Ω. Since the V_H values assumed at $B = \pm 25$ mT depend on s and T and thus on V_S and V_T, these two surfaces can be parameterized as $\boldsymbol{v}_\pm(V_S, V_T) = (V_H(B = \pm 25 \text{ mT}, V_S, V_T), V_S, V_T)$, where $+$ and $-$ denote the top and
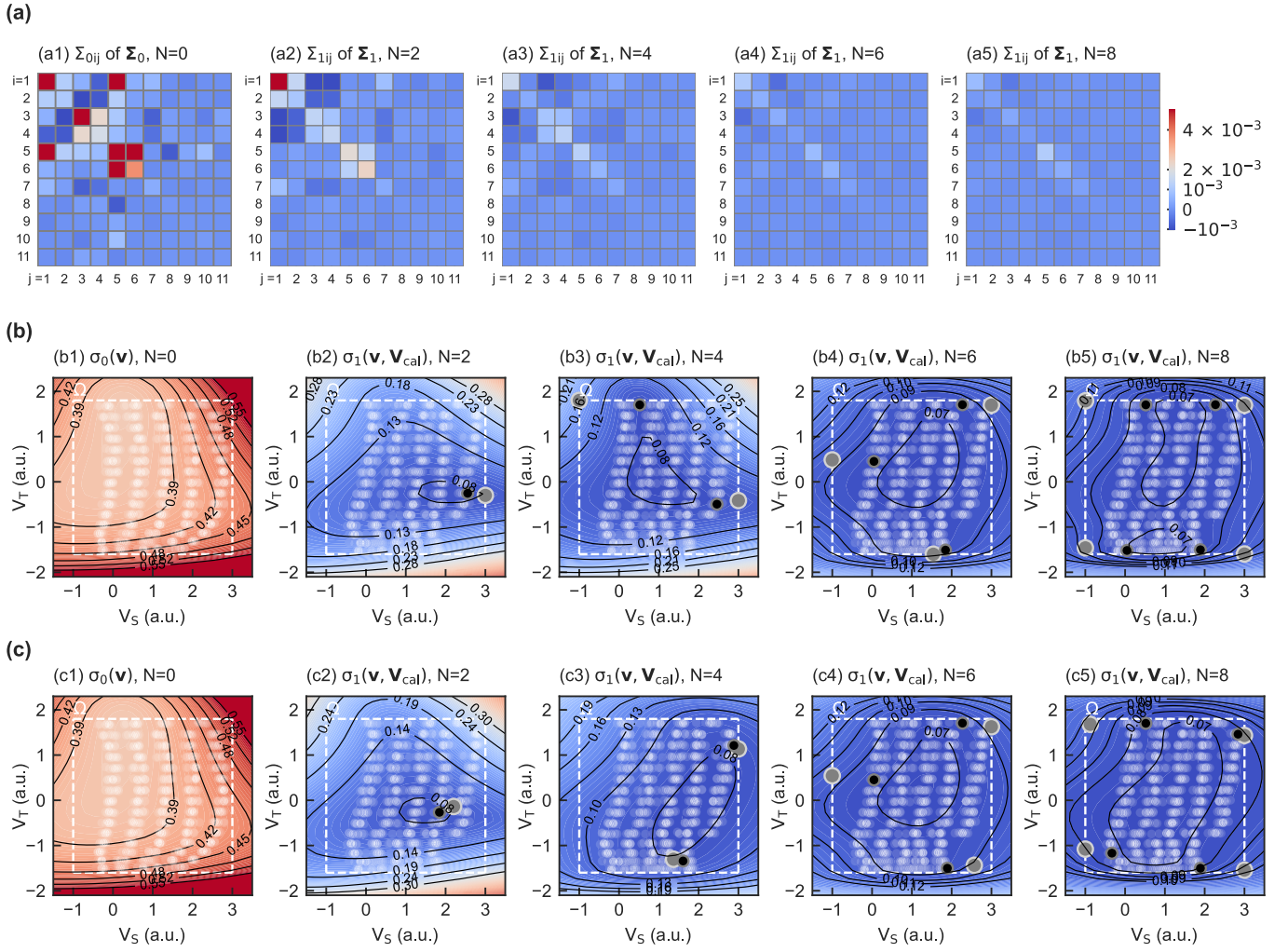
Fig. 6. (a) Covariance matrices, G-optimality. (b) Confidence intervals, G-optimality. (c) Confidence intervals, I-optimality. (a1) Elements Σ_{0ij} of the prior covariance matrix $\mathbf{\Sigma}_0$ and (b1) and (c1) prior confidence interval quantified by σ_0. White semitransparent dots show the characterization data of a representative prior-generating specimen; white dashed line delimits Ω in the (V_S, V_T)-plane. The improved sensor accuracy after calibration with (a2) $N = 2$, (a3) $N = 4$, (a4) $N = 6$, and (a5) $N = 8$ calibration conditions is visualized by the progressive shrinkage of the posterior covariance matrix $\mathbf{\Sigma}_1$. Posterior confidence intervals inferred for a representative validation specimen, as quantified by σ_1, after near-optimal calibrations with $N = 2, 4, 6$, and 8 subject to (b2)–(b5) G-optimality and (c2)–(c5) I-optimality. Gray dots denote the ideal calibration conditions $(V_{S\min}, V_{T\min})$, while the black dots show the representative validation specimen's output signals V_{cal} obtained under the near-optimal calibration conditions. The white semitransparent dots show the entire set of validation data for the representative specimen. The heat plots [(b1)–(c5)] share the same color scale.

bottom surfaces, respectively. The search is therefore carried out in the 2-D region delimited by $-1 \leq V_S \leq 3$ and $-1.6 \leq V_T \leq 1.8$. One has to be aware that for each combination of V_S and V_T identified as an adequate calibration condition, a pair of calibration measurements is carried out, namely, at $B = \pm 25$ mT. Switching B requires only the Helmholtz coil current to be inverted, which is fast and thus efficient.

In what follows, the procedure is illustrated in detail for $N = 2$. In other words, a single optimal calibration combination of $(V_{S\min}, V_{T\min})$ is to be identified. For this purpose, we define $\mathbf{V} = (\mathbf{v}_-(V_S, V_T), \mathbf{v}_+(V_S, V_T))$. Therefore, $\sigma_1(\mathbf{v}, \mathbf{V})$ is obtained using (8) and (10). This then serves to evaluate $f_G(\mathbf{V})$ and $f_I(\mathbf{V})$ [cf. (11) and (13)]. The two objective functions are shown in Fig. 7 as a function of the two variables V_S and V_T of $\mathbf{V}$. Their minima were identified numerically in Python using the SciPy library [89]. The optimal calibration conditions $(V_{S\min}, V_{T\min})$ are shown as gray dots, while the

white dashed line delimits the search domain. These values are $(3, -0.3)$ for G-optimality and $(2.2, -0.14)$ for I-optimality.

The next task is to identify calibration loads F and T able to elicit response signals $(V_{S\text{cal}}, V_{T\text{cal}})$ from any specimen near the ideal values $(V_{S\min}, V_{T\min})$. By analysis of the prior-generation data and the loads applied there, $F = 20$ N and $T = 20\,°\text{C}$ are concluded to be a reasonable choice for G-optimality, whereas $F = 15$ N and $T = 20\,°\text{C}$ are for I-optimality. Under these near-optimal loads, calibration output signals $\mathbf{V}_{cal}$ are recorded from a specimen being calibrated. Based on $\mathbf{V}_{cal}$ and $\mathbf{B}_{cal} = (-25\text{ mT}, 25\text{ mT})^\top$, one deduces $B_1(\mathbf{v}, \mathbf{V}_{cal}, \mathbf{B}_{cal}) = \boldsymbol{\phi}(\mathbf{v})^\top \mathbf{w}_1(\mathbf{V}_{cal}, \mathbf{B}_{cal})$ and $\sigma_1^2(\mathbf{v}, \mathbf{V}_{cal})$ of the sensor, using (7)–(10).

Fig. 6(a2) symbolizes the posterior covariance matrix $\mathbf{\Sigma}_1$ of a representative validation specimen after near-G-optimal calibration at $\mathbf{V}_{cal}$. The corresponding confidence interval, as quantified by $\sigma_1(\mathbf{v}, \mathbf{V}_{cal})$ on the top surface of Ω, is

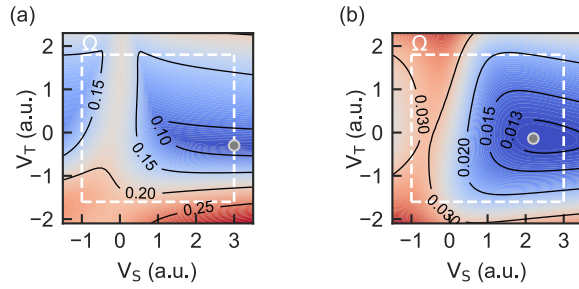Fig. 7. (V_S, V_T) dependence of the objective functions for (a) G-optimality [f_G (mT^2)] and (b) I-optimality [f_I (mT^2)] for calibration at a single stress–temperature condition. The white dashed line delimits Ω. The minima, indicated by gray dots, define the respective calibration conditions (V_{Smin}, V_{Tmin}).

shown in Fig. 6(b2), again as a function of V_S and V_T. The optimal calibration condition (V_{Smin}, V_{Tmin}) is indicated by the gray dot, while the near-optimal condition is indicated by the black dot. The white dashed boarder again delimits Ω. The semitransparent white dots show sensor output signals (V_S, V_T) of the representative specimen under the same set of load conditions as applied during characterization of the prior-generating specimens. These actual output data, including corresponding V_H values for $B = -25, 0$, and 25 mT, are used for the comparison of actual data with the predictive response $B_1(\boldsymbol{v}, \boldsymbol{V}_{cal}, \boldsymbol{B}_{cal})$ and thus for the validation of the method in Section IV-D. Similar to Fig. 6(b2), Fig. 6(c2) shows σ_1 as inferred from near-I-optimal calibration of the same validation specimen.

Finally, optimal and near-optimal calibration strategies with $N > 2$ load conditions are analyzed. We considered $N = 4, 6$, and 8, implying combinations of 2, 3, and 4 (F, T) conditions, respectively. At each condition, measurements are carried out with applied $B = \pm 25$ mT. Results are shown in the last three columns of Fig. 6. The heat plots in Fig. 6(a3)–(a5) again symbolize the resulting $\boldsymbol{\Sigma}_1$ of the updated probability distribution of $\boldsymbol{w}$. These matrices are obtained for measurements performed at the optimal calibration conditions indicated by the two [Fig. 6(a3)], three [Fig. 6(a4)], and four [Fig. 6(a5)] gray dots in Fig. 6(b3)–(b5), respectively. Like for $N = 2$, these optimal conditions were determined numerically using a search algorithm programmed in Python and taking advantage of the SciPy library [89]. Actual calibration data of a representative validation specimen were obtained under near-optimal conditions indicated by the black dots. These substitute conditions were again selected based on the prior characterization data, as described for $N = 2$. The contour plots show the resulting (V_S, V_T)-dependent updated predictive confidence interval defined by σ_1 derived from near-optimal calibration conditions $\boldsymbol{V}_{cal}$. These are again the values of σ_1 on the top boundary of Ω.

The results in Fig. 6(c3)–(c5) are similar to those in Fig. 6(b3)–(b5). However, like those in (c2), they were obtained with the aim of I-optimal calibration.

D. Validation

For the purpose of calibration strategy validation, the 15 validation specimens were submitted to the same characterization
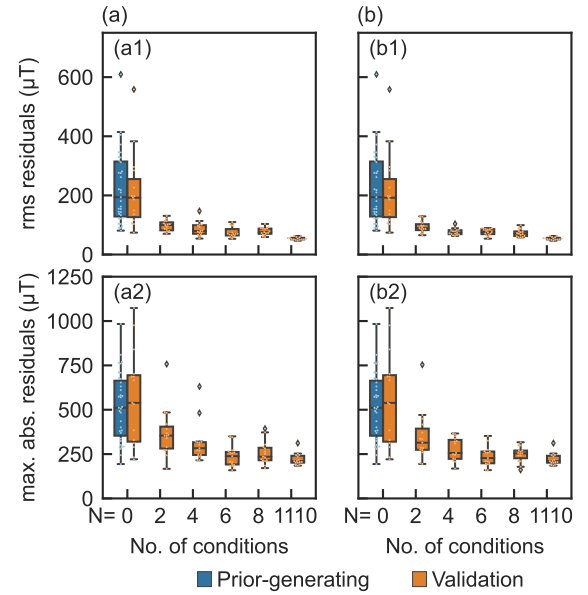

Fig. 8. Top half: rms residual values (light-colored dots) and corresponding box plots for the 15 validation specimens after calibration based on (a) G-optimality and (b) I-optimality for calibration with $N = 2, 4, 6$, and 8 near-optimal measurements and characterization using 1110 measurements. Distributions of the corresponding maximum absolute residuals are shown in the lower half. For $N = 0$, the plots also show the corresponding results for the 35 prior-generating specimens.

procedure as the prior-generating specimens, as described in Section III-C. Per validation specimen, this results in a set of 1110 data triples $\boldsymbol{v} = (V_H, V_S, V_T)$ with the corresponding applied B values. The set of validation data of a representative validation specimen is shown in Fig. 6(b2)–(b5) and (c2)–(c5).

For each validation specimen, we compute the 1110 residuals $B_0 - B$ for $N = 0$ and $B_1 - B$ for the cases $N = 2, 4, 6$, and 8 discussed in Section IV-C and for $N = 1110$. The latter case means that the Bayesian update is performed with all available data.

Accuracies of the validation specimens before and after calibration are shown by orange box plots in Fig. 8. After near-G-optimal calibration, the distribution of the rms residuals of the 15 validation specimens is shown in Fig. 8(a1), while the distribution of the maximum absolute residuals is reported in Fig. 8(a2). Fig. 8(b1) and (b2) summarizes the corresponding observed accuracies after near-I-optimal calibrations of the validation specimens. For $N = 0$, the distributions of the rms and maximum absolute residuals computed for the prior-generating specimens are reported as well by blue-colored box plots.

Furthermore, the fraction of residuals lying within the $\pm \sigma_1$-interval of the inferred B values, i.e., B_0 for $N = 0$ and B_1 for all other N, has been computed. In its top section, Fig. 9 shows these fractions for G- and I-optimality. Orange bars represent again the validation specimens, whereas blue bars result from the prior-generating specimens.

In addition, for each specimen and each abovementioned N value, $f_G^{1/2}(\boldsymbol{V}_{cal})$ and $f_I^{1/2}(\boldsymbol{V}_{cal})$ are computed using (11) and (13). These quantify the maximum and rms predictive uncertainties resulting from the prior ($N = 0$) and updated ($N = 2, 4, 6, 8$, and 1110) knowledge about the specimens.
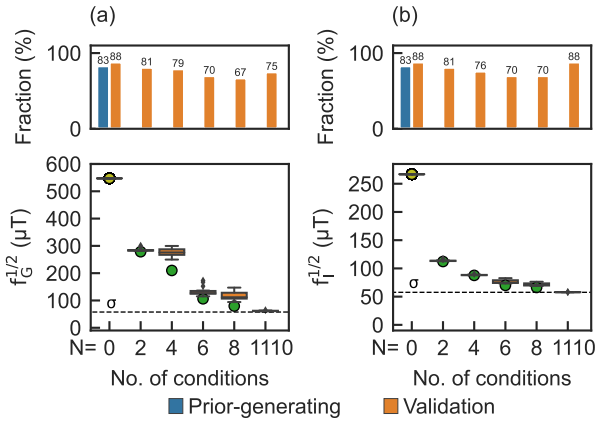
Fig. 9. *N*-dependence of the objective functions (a) f_G (G-optimality) and (b) f_I (I-optimality). For $N = 0$, values obtained with σ_0 are shown as olive-colored dots. Green dots show the values obtained under 2, 4, 6, and 8 ideal calibration conditions. The box plots show the distributions of values obtained by corresponding near-optimal calibrations of the 15 validation specimens. The upper two plots show the fractions of the residuals of the entire datasets of the specimens within the respective $\pm \sigma_0$ ($N = 0$) and $\pm \sigma_1$ ($N = 2, 4, 6$, and 8) confidence intervals (blue: prior generation and orange: validation).

The lower part of Fig. 9 shows the results. The olive-colored dots show the values derived from $\sigma_0^2(\boldsymbol{v})$, while the green dots show the corresponding values obtained with $\sigma_1^2(\boldsymbol{v}, \boldsymbol{V}_{\min})$ after optimal calibration. The box plots show the distributions of $f_G^{1/2}$ and $f_I^{1/2}$ after individual near-optimal calibrations of the validation specimens, using $\sigma_1(\boldsymbol{v}, \boldsymbol{V}_{\text{cal}})$.

V. DISCUSSION

For the first time, a Hall–stress–temperature sensor system was calibrated against two cross-sensitivities by means of Bayesian calibration. The calibration was carried out with fewer measurements than model parameters. For a sensor model with $M = 11$ parameters, the method was demonstrated by calibrations using $N = 2, 4, 6$, and 8 measurements requiring only one, two, three, and four force–temperature (F, T) pairs as calibration conditions. All identified G- and I-optimal calibration strategies allow an unknown B pervading calibrated sensors to be inferred from the sensor system's output signals V_H, V_S, and V_T with known accuracy. The accuracy increases with N, as shown in Figs. 6, 8, and 9.

Near-G-optimal calibrations lead to a progressive refinement of the covariance matrix with each additional (F, T) calibration condition [cf. Fig. 6(a1)–(a5)]. The refinement of $\boldsymbol{\Sigma}_1$ entails a corresponding shrinking of the uncertainty σ_1 within the operating range Ω of accordingly calibrated specimens and hence allows a more accurate inference of B from the signals. For example, the maxima σ_1 on the top surface of Ω after a single (F, T) calibration under G-optimal [cf. Fig. 6(b2)] and I-optimal [cf. Fig. 6(c2)] conditions are smaller than the minimum of σ_0 before calibration [cf. Fig. 6(b1) and (c1)]. With increasing N, the uncertainty shrinks further, as shown in Fig. 6(b1)–(c5). A salient feature of Bayesian sensor calibration in comparison with nonprobabilistic approaches is that it not only allows to infer B from the sensor signals but simultaneously also provides the uncertainty of the inferred

B value. It does so by providing the standard deviation σ_1 within Ω and even beyond its boundaries.

Figs. 6(b2) and (c2) and 7 show the G- and I-optimal calibration conditions found for a single (F, T) calibration condition as gray dots. It is noteworthy in both cases that the near-optimal calibration within the grid of (F, T) conditions defined in Section III-C is performed at $T = 20$ °C. Calibration close to room temperature is favorable from an economic point of view. It is interesting to know whether the near-optimal conditions $F = 20$ N (G-optimality) and $F = 15$ N (I-optimality) can be replaced without significant loss by the more economical $F = 0$ N. This can be assessed using the validation data. We conclude that the maximum σ_1 increases to about 428 μT from about 283 μT in the near-optimal case. Similarly, the rms σ_1 increases to 160 μT from 113 μT. In conclusion, it is advisable in this case to apply a nonzero force to ensure proper stress compensation.

The posterior accuracy is now evaluated in terms of the residuals of the 15 validation specimens. In the following, the focus is on rms residuals after I-optimal calibrations reported in Fig. 8(b1). Two outliers among the $15 \times 6 = 90$ rms values, indicated by the diamond symbols, are neglected. The figure shows the distribution of the rms residuals and describes the tradeoff between absolute accuracy and calibration effort as a function of N. Before calibration and based on the prior knowledge alone, the rms residuals were found to be 74–383 μT, corresponding to relative errors of 0.3%–1.5% in comparison with the maximum B value of 25 mT. After calibration at the near-I-optimal single (F, T) condition, the rms residuals were reduced to 65–129 μT, i.e., 0.26%–0.52%. With increasing (F, T) conditions, only small further improvements to 63–89 μT ($N = 4$), 53–90 μT ($N = 6$), and 58–99 μT ($N = 8$) are achieved. It is noteworthy that near-I-optimal calibration with $N = 2$ allowed to significantly reduce the inaccuracy of the outlier in Fig. 8(b1) for $N = 0$. It is captured by the upper whisker. By a thorough calibration with $N = 1110$, the residuals are further reduced to 47–63 μT (0.19%–0.25%). This is only a minor further improvement considering the additional effort.

In [80], a non-Bayesian calibration of 20 Hall–stress–temperature sensor systems provided an accuracy of 149 (0.5%) and 236 μT (0.79%) using $N = 570$ and $N = 6$ measurements, respectively, for B values in the range of ± 30 mT. A polynomial model comprising six parameters was used to infer the magnetic induction B for temperatures between -40 °C and 125 °C and mechanical stress values comparable to those applied here. In conclusion, the accuracy achieved in the present Bayesian study after calibration with $N = 2$ exceeds that of the non-Bayesian case in [80] with $N = 6$ by a factor of 1.5–3.

The continuous reduction of both objective functions, f_G and f_I, with increasing N is apparent from Fig. 9. It confirms that the Bayesian optimal calibration design is effective and works with smaller numbers of calibration measurements than model parameters. In the following, we discuss the N-dependent uncertainty left by the calibration based on the 15 $f_I^{1/2}$ values (i.e., the 15 values of the rms σ_1 in Ω) for the near-I-optimal calibrations in Fig. 9(b) again neglecting

the outliers. For comparison, the rms σ_0 in Ω is 267 μT. After a single (F, T) calibration ($N = 2$), the 15 $f_I^{1/2}$ values are reduced to 112–114 μT. Thereafter, like the residuals (cf. Fig. 8), they are only slightly further reduced to 87–89 μT ($N = 4$), 73–83 μT ($N = 6$), and 68–77 μT ($N = 8$). When all available data ($N = 1110$) are used, a further reduction to 57.9–58 μT close to $\sigma = 57.7$ μT is achieved. A similar observation was found in [4]. After 14 Hall–temperature sensor systems were calibrated at two temperatures near the I-optimum, their uncertainty was reduced from 203 (rms σ_0) to 41 μT (rms σ_1). In comparison, the more complex model in the present study additionally ensures the stress compensation and therefore demands a more substantial calibration effort in order to achieve a similar accuracy. In [6], similar observations were made regarding the accuracy improvement after a Bayesian calibration of temperature-sensitive pressure sensors. This study used a polynomial model with five model parameters and determined calibration conditions in terms of I-optimality.

The application of near-optimal (F, T) calibration conditions produces sensor signals V_{cal} differing from the identified optimum V_{min} minimizing f_G or f_I. The optimal f_G and f_I values are represented by green dots in Fig. 9, while the boxes include the corresponding values obtained with near-optimal V_{cal} values. All experimental values in Fig. 9 closely follow the theoretical optimal values. Consequently, near-optimal calibration strategies were obviously identified. Nevertheless, how to select a near-optimal (F, T) pair of conditions for a given (V_{Smin}, V_{Tmin}) will likely depend on the required sensor specification in view of its application and may also be subject to the question of cost-effectiveness.

The decision to rely on $Q = 35$ specimens for the prior generation was taken in view of the complexity of the model with its $M = 11$ parameters. With $MQ = 385$ prior-generating data, the information available to determine the symmetric Σ_0 was significantly larger than the number of its independent entries, namely, $M(M + 1)/2 = 66$. Compared to the study in [4], where $Q = 14$ and $M = 7$, the ratio of available prior information to independent entries of Σ_0 was chosen here to be even larger, namely, $385/66 \approx 5.8$ in comparison with $98/28 = 3.5$ in order to ensure a trustworthy prior. However, the question of how far the multivariate normal distribution described by (3) and (4) is a trustworthy approximation of the subjacent multivariate student distribution [4] remains open at this point and deserves a dedicated thorough study.

Nevertheless, in the context of this question, it is remarkable that in all calibration cases, as highlighted by the top of Fig. 9, more than 67% of the applied B values lie within the $\pm\sigma_1$-interval of the B value inferred from the sensor signals. This is close to 68.3%, the well-known cumulative probability within the $\pm 1\sigma_1$ range of a Gaussian around its mean. We interpret this as evidence that the prior probability distribution of w estimated from the prior-generating specimens using (3) and (4) provides a reasonable picture of the actual w distribution of the sensor ensemble.

The formalism described in Section II and applied here to the special case of Hall sensors is applicable whenever the measurand of a sensor system is well modeled by a response function of the form $\phi(x)^\top w$ linear in the model parameters w, where x denotes the independent variables. There is no fundamental restriction regarding the set of basis functions $\phi(x)$. Sensor types that may benefit from Bayesian sensor calibration in the present form include ion-selective chemical sensors [90], [91], inertial sensors [22], [23], [92], and mechanical sensors [5], [8], [10], [17], [18], [93]. By using the method of multivariate Bayesian regression and inference [77], [88], we expect the method to be generalizable to multisensor systems designed to provide values of more than a single measurand. Sensors modeled by more complex response functions nonlinearly involving some model parameters, such as chemical sensors, do not preclude the application of Bayesian methods. However, the mathematics will no longer boil down to matrix calculus and likely entail heavier computations [76], [77], [88]. In these cases and others without available explicit models, ANNs may be helpful [67], [68].

VI. CONCLUSION

In this article, the method of Bayesian sensor calibration was successfully applied to a multisensor system affected by two parasitic sensitivities. Bayesian calibration of the investigated Hall–stress–temperature sensor system guarantees a satisfying accuracy even when relying on fewer calibration measurements ($N = 2, 4, 6,$ and 8) than model parameters ($M = 11$). For comparison, a thorough calibration with a set of $N = 1110$ conditions leads to a median residual of 0.21% referred to $B = 25$ mT. This is only 0.07% better than a calibration using six measurements. A second strength of the Bayesian approach to sensor calibration is that it enables to predict the accuracy resulting from calibration. The validity of the accuracy predictions was experimentally verified. The accuracy of the validation specimens after parsimonious calibration was indeed found to be as predicted. The ability to predict the accuracy of specimens after calibration distinguishes the Bayesian approach from ANN-based ML algorithms, where the trustworthiness of the trained ANN, instead of being confirmed, is established by testing it using independent data [14], [71], [76], [94], [95].

The successful reduction of calibration conditions still ensuring competitive accuracy is rooted in the prior distribution of sensor model parameters. A fundamental requirement for establishing such useful prior knowledge is that the specimens belong to an ensemble of sensor systems with a reasonably narrow distribution of response parameters. In the present case, this is ensured at the technology and hardware levels by a commercial standard 180-nm CMOS process of X-Fab Silicon Foundries (Erfurt, Germany) for the fabrication and by a sophisticated sensor design [30]. It is clear that the effort needed to acquire the prior database is intense and represents a weighty factor in the total calibration cost. However, the parsimony of the reduced calibration schemes building upon the prior allows to save costs, possibly over entire production volumes. Whether the Bayesian approach is able to offer a net cost saving in some calibration task will depend on aspects extending beyond the limits of purely scientific questions.

TABLE I
SETS OF BASIS FUNCTIONS OF MODEL NOS. 1 TO 15 WITH
M MODEL PARAMETERS. MODEL NO. 9 HAS BEEN
SELECTED IN THE PRESENT STUDY

Model no.	M	Basis functions $\phi(v)$
1	7	$\{1, V_T,$ $V_H, V_H V_T, V_H V_T^2, V_H V_T^3, V_H V_T^4\}$
2	8	$\{1, V_T, V_S,$ $V_H, V_H V_T, V_H V_T^2, V_H V_T^3, V_H V_T^4\}$
3	9	$\{1, V_T, V_S, V_S V_T,$ $V_H, V_H V_T, V_H V_T^2, V_H V_T^3, V_H V_T^4\}$
4	8	$\{1, V_T,$ $V_H, V_H V_T, V_H V_T^2, V_H V_T^3, V_H V_T^4, V_H V_S\}$
5	9	$\{1, V_T, V_S,$ $V_H, V_H V_T, V_H V_T^2, V_H V_T^3, V_H V_T^4, V_H V_S\}$
6	10	$\{1, V_T, V_S, V_S V_T,$ $V_H, V_H V_T, V_H V_T^2, V_H V_T^3, V_H V_T^4, V_H V_S\}$
7	9	$\{1, V_T,$ $V_H, V_H V_T, V_H V_T^2, V_H V_T^3, V_H V_T^4, V_H V_S, V_H V_S V_T\}$
8	10	$\{1, V_T, V_S,$ $V_H, V_H V_T, V_H V_T^2, V_H V_T^3, V_H V_T^4, V_H V_S, V_H V_S V_T\}$
9	11	$\{1, V_T, V_S, V_S V_T,$ $V_H, V_H V_T, V_H V_T^2, V_H V_T^3, V_H V_T^4, V_H V_S, V_H V_S V_T\}$
10	9	$\{1, V_T,$ $V_H, V_H V_T, V_H V_T^2, V_H V_T^3, V_H V_T^4, V_H V_S, V_H V_S^2\}$
11	10	$\{1, V_T, V_S,$ $V_H, V_H V_T, V_H V_T^2, V_H V_T^3, V_H V_T^4, V_H V_S, V_H V_S^2\}$
12	11	$\{1, V_T, V_S, V_S V_T,$ $V_H, V_H V_T, V_H V_T^2, V_H V_T^3, V_H V_T^4, V_H V_S, V_H V_S^2\}$
13	10	$\{1, V_T,$ $V_H, V_H V_T, V_H V_T^2, V_H V_T^3, V_H V_T^4, V_H V_S, V_H V_S V_T, V_H V_S^2\}$
14	11	$\{1, V_T, V_S,$ $V_H, V_H V_T, V_H V_T^2, V_H V_T^3, V_H V_T^4, V_H V_S, V_H V_S V_T, V_H V_S^2\}$
15	12	$\{1, V_T, V_S, V_S V_T,$ $V_H, V_H V_T, V_H V_T^2, V_H V_T^3, V_H V_T^4, V_H V_S, V_H V_S V_T, V_H V_S^2\}$

APPENDIX

Table I lists the 15 polynomial basis functions $\phi(v)$ used to model the magnetic induction B as a function of V_H, V_S, and V_T. The models are systematically arranged in five triplets, namely $(1, 2, 3)$, $(4, 5, 6)$, ..., $(13, 14, 15)$. Each triplet has the same set of basis functions modeling $1/S_A$ and an increasing number of basis functions modeling B_{off}. The first model, no. 1, uses the same basis functions as in [4] and has no polynomial terms in V_S. For models 2 and 3, the terms V_S and V_S, $V_S V_T$ are added to 1 and V_T, respectively. The same principle applies to all further triplets of basis functions where the basis functions modeling $1/S_A$ are progressively expanded. For example, the triplet $(4, 5, \text{and } 6)$ has the additional term $V_H V_S$ in comparison with the triplet $(1, 2, \text{and } 3)$, while the terms for modeling B_{off} are the same.

ACKNOWLEDGMENT

REFERENCES

[1] I. N. Cholakova, T. B. Takov, R. T. Tsankov, and N. Simonne, "Temperature influence on Hall effect sensors characteristics," in *Proc. 20th Telecommun. Forum (TELFOR)*, Nov. 2012, pp. 967–970.

[2] S. Huber, A. Laville, C. Schott, and O. Paul, "A bridge-type resistive temperature sensor in CMOS technology with low stress sensitivity," in *Proc. IEEE SENSORS*, Valencia, Spain, Nov. 2014, pp. 1455–1458.

[3] S. H. Lindenberger, "Active stabilization of the magnetic sensitivity in CMOS Hall sensors," Ph.D. thesis, Dept. Microsyst. Eng. (IMTEK), Univ. Freiburg, Breisgau, Germany, 2017. [Online]. Available: https://freidok.uni-freiburg.de/fedora/objects/freidok:11568/datastreams/FILE1/content

[4] M. Berger, C. Schott, and O. Paul, "Bayesian sensor calibration," *IEEE Sensors J.*, vol. 22, no. 20, pp. 19384–19399, Oct. 2022.

[5] M. Akbar and M. A. Shanblatt, "Temperature compensation of piezoresistive pressure sensors," *Sens. Actuators, A. Phys.*, vol. 33, no. 3, pp. 155–162, 1992.

[6] S. B. Crary and Y. Jeong, "Bayesian optimal design of experiments for sensor calibration," in *Proc. Int. Solid-State Sens. Actuators Conf.*, Stockholm, Sweden, Jun. 1995, pp. 48–51.

[7] M. Aryafar, M. Hamedi, and M. M. Ganjeh, "A novel temperature compensated piezoresistive pressure sensor," *Measurement*, vol. 63, pp. 25–29, Mar. 2015.

[8] S. Huber, C. Schott, and O. Paul, "Package stress monitor to compensate for the piezo-Hall effect in CMOS Hall sensors," *IEEE Sensors J.*, vol. 13, no. 8, pp. 2890–2898, Aug. 2013.

[9] J. L. Ramirez and F. Fruett, "Integrated octagonal mechanical stress sensor with temperature compensation," *IEEE Sensors J.*, vol. 18, no. 14, pp. 5707–5714, Jul. 2018.

[10] M. O. Kayed, A. A. Balbola, E. Lou, and W. A. Moussa, "Development of doped silicon multi-element stress sensor rosette with temperature compensation," *IEEE Sensors J.*, vol. 20, no. 3, pp. 1176–1183, Feb. 2020.

[11] R. S. Popovic, *Hall Effect Devices*, 2nd ed. London, U.K.: Institute of Physics Publishing, 2004.

[12] S. Dey, S. Santra, S. K. Ray, and P. K. Guha, "Coral-like $Cu_x Ni_{(1-x)}O$-based resistive sensor for humidity and VOC detection," *IEEE Sensors J.*, vol. 18, no. 15, pp. 6078–6084, Aug. 2018.

[13] Y. Vlasov, A. Legin, and A. Rudnitskaya, "Cross-sensitivity evaluation of chemical sensors for electronic tongue: Determination of heavy metal ions," *Sens. Actuators B, Chem.*, vol. 44, nos. 1–3, pp. 532–537, 1997.

[14] T. Hayasaka et al., "An electronic nose using a single graphene FET and machine learning for water, methanol, and ethanol," *Microsyst. Nanoeng.*, vol. 6, no. 1, p. 50, 2020, doi: 10.1038/s41378-020-0161-3.

[15] W. Qu and W. Wlodarski, "A thin-film sensing element for ozone, humidity and temperature," *Sens. Actuators B, Chem.*, vol. 64, nos. 1–3, pp. 42–48, Jun. 2000.

[16] C. Cantalini et al., "Cross sensitivity and stability of NO_2 sensors from WO_3 thin film," *Sens. Actuators B, Chem.*, vol. 35, nos. 1–3, pp. 112–118, 1996.

[17] F. Becker and O. Paul, "Efficient cross-sensitivity compensation in multisensor systems by half-blind calibration," *Sens. Actuators A, Phys.*, vol. 257, pp. 154–164, Apr. 2017.

[18] F. Becker, R. Jäeger, F. Schmidt, B. Lapatki, and O. Paul, "Miniaturized six-degree-of-freedom force/moment transducers for instrumented teeth," *IEEE Sensors J.*, vol. 17, no. 12, pp. 3644–3655, Jun. 2017.

[19] F. Becker, B. Lapatki, and O. Paul, "Miniaturized six-degree-of-freedom force/moment transducers for instrumented teeth with single sensor chip," *IEEE Sensors J.*, vol. 18, no. 6, pp. 2268–2277, Mar. 2018.

[20] E. Tatar, S. E. Alper, and T. Akin, "Quadrature-error compensation and corresponding effects on the performance of fully decoupled MEMS gyroscopes," *J. Microelectromech. Syst.*, vol. 21, no. 3, pp. 656–667, Jun. 2012.

[21] B. E. Uzunoglu, D. Erkan, and E. Tatar, "A ring gyroscope with on-chip capacitive stress compensation," *J. Microelectromech. Syst.*, vol. 31, no. 5, pp. 741–752, Oct. 2022.

[22] C. Jurgschat, F. Roewer, I. Toth, T. Ohms, and A. Zimmermann, "Integrated stress sensors for humidity performance drift analysis and compensation in inertial measurement units," *J. Microelectromech. Syst.*, vol. 31, no. 6, pp. 918–926, Dec. 2022.

[23] I. Skog and P. Händel, "Calibration of a MEMS inertial measurement unit," in *Proc. XVII IMEKO World Congr.*, Rio de Janeiro, Brazil, 2006, pp. 1–6.

[24] W. Fong, S. Ong, and A. Nee, "Methods for in-field user calibration of an inertial measurement unit without external equipment," *Meas. Sci. Technol.*, vol. 19, no. 8, 2008, Art. no. 085202.

[25] D. W. Braudaway, "The costs of calibration," *IEEE Trans. Instrum. Meas.*, vol. 52, no. 3, pp. 738–741, Jun. 2003.

[26] J. Fraden, "Calibration," in *Handbook of Modern Sensors: Physics, Designs, and Applications*, 3rd ed. New York, NY, USA: Springer, 2004, ch. 2, pp. 18–19.

[27] G. van der Horn and J. H. Huijsing, "Integrated smart sensor calibration," in *Smart Sensor Interfaces*, J. H. Huijsing and G. C. M. Meijer, Eds. Boston, MA, USA: Springer, 1997, pp. 45–60, doi: 10.1007/978-1-4615-6061-6_5.

[28] A. Miquel-Ibarz, J. Burgués, and S. Marco, "Global calibration models for temperature-modulated metal oxide gas sensors: A strategy to reduce calibration costs," *Sens. Actuators B, Chem.*, vol. 350, Jan. 2022, Art. no. 130769.

[29] M. Shoaib, N. H. Hamid, A. F. Malik, N. B. Zain Ali, and M. Tariq Jan, "A review on key issues and challenges in devices level MEMS testing," *J. Sensors*, vol. 2016, Feb. 2016, Art. no. 1639805.

[30] S. Leroy, S. Rigert, A. Laville, A. Ajbl, and G. F. Close, "Integrated Hall-based magnetic platform for position sensing," in *Proc. 43rd IEEE Eur. Solid State Circuits Conf. (ESSCIRC)*, Sep. 2017, pp. 360–363.

[31] R. S. Popovic, "The vertical Hall-effect device," *IEEE Electron Device Lett.*, vol. EDL-5, no. 9, pp. 357–358, Sep. 1984.

[32] C. Schott, P.-A. Besse, and R. S. Popovic, "Planar Hall effect in the vertical Hall sensor," *Sens. Actuators A, Phys.*, vol. 85, nos. 1–3, pp. 111–115, Aug. 2000.

[33] C. Roumenin, K. Dimitrov, and P. Tzvetkov, "Vertical Hall effect devices in the basis of smart silicon sensors," in *Proc. IEEE Intell. Data Acquisition Adv. Comput. Syst., Technol. Appl.*, Sep. 2005, pp. 55–58.

[34] C. Sander, C. Leube, and O. Paul, "Novel compact two-dimensional CMOS vertical Hall sensor," in *Proc. Transducers-18th Int. Conf. Solid-State Sensors, Actuat. Microsyst. (TRANSDUCERS)*, Jun. 2015, pp. 1164–1167.

[35] C. Sander et al., "Fully symmetric vertical Hall devices in CMOS technology," in *Proc. IEEE SENSORS*, Nov. 2013, pp. 15–18.

[36] R. Racz, C. Schott, and S. Huber, "Electronic compass sensor," in *Proc. IEEE Sensors*, 2004, pp. 1446–1449.

[37] F. Burger, P.-A. Besse, and R. S. Popovic, "New fully integrated 3-D silicon Hall sensor for precise angular-position measurements," *Sens. Actuators A, Phys.*, vol. 67, nos. 1–3, pp. 72–76, May 1998.

[38] C. Schott, D. Manic, and R. S. Popovic, "Microsystem for high-accuracy 3-D magnetic-field measurements," *Sens. Actuators A, Phys.*, vol. 67, nos. 1–3, pp. 133–137, May 1998.

[39] C. Sander, C. Leube, T. Aftab, P. Ruther, and O. Paul, "Isotropic 3D silicon Hall sensor," in *Proc. 28th IEEE Int. Conf. Micro Electro Mech. Syst. (MEMS)*, Jan. 2015, pp. 893–896.

[40] C. Sander, C. Leube, T. Aftab, P. Ruther, and O. Paul, "Monolithic isotropic 3D silicon Hall sensor," *Sens. Actuators A, Phys.*, vol. 247, pp. 587–597, Aug. 2016.

[41] D. Manic, J. Petr, and R. S. Popovic, "Temperature cross-sensitivity of Hall plate in submicron CMOS technology," *Sens. Actuators A, Phys.*, vol. 85, no. 1, pp. 244–248, 2000.

[42] B. Hälg, "Piezo-Hall coefficients of n-type silicon," *J. Appl. Phys.*, vol. 64, no. 1, pp. 276–282, 1988.

[43] Y. Kanda and Y. Kanda, "A graphical representation of the piezoresistance coefficients in silicon," *IEEE Trans. Electron Devices*, vol. ED-29, no. 1, pp. 64–70, Jan. 1982.

[44] Y. Kanda, "Piezoresistance effect of silicon," *Sens. Actuators A, Phys.*, vol. 28, no. 2, pp. 83–91, 1991.

[45] U. Ausserlechner, M. Motz, and M. Holliber, "Compensation of the Piezo-Hall effect in integrated Hall sensors on (100)-Si," *IEEE Sensors J.*, vol. 7, no. 11, pp. 1475–1482, Nov. 2007.

[46] Y. Zou, J. C. Suhling, R. C. Jaeger, and H. Ali, "Three dimensional die surface stress measurements in delaminated and non-delaminated plastic packages," in *Proc. 48th Electron. Compon. Technol. Conf.*, May 1998, pp. 1223–1234.

[47] J. H. Lau, Ed., *Thermal Stress and Strain in Microelectronics Packaging*. New York, NY, USA: Springer, 1993, doi: 10.1007/978-1-4684-7767-2.

[48] S. Fischer, H. Beyer, R. Janke, and J. Wilde, "The influence of package-induced stresses on moulded Hall sensors," *Microsyst. Technol.*, vol. 12, nos. 1–2, pp. 69–74, 2005.

[49] S. Fischer, T. Fellner, J. Wilde, H. Beyer, and R. Janke, "Analyzing parameters influencing stress and drift in moulded Hall sensors," in *Proc. 1st Electron. Systemintegr. Technol. Conf.*, Sep. 2006, pp. 1378–1385.

[50] E. Stellrecht, B. Han, and M. G. Pecht, "Characterization of hygroscopic swelling behavior of mold compounds and plastic packages," *IEEE Trans. Compon. Packag. Technol.*, vol. 27, no. 3, pp. 499–506, Sep. 2004.

[51] J. C. Suhling and R. C. Jaeger, "Silicon piezoresistive stress sensors and their application in electronic packaging," *IEEE Sensors J.*, vol. 1, no. 1, pp. 14–30, Jun. 2001.

[52] U. Ausserlechner, M. Motz, and M. Holliber, "Drift of magnetic sensitivity of smart Hall sensors due to moisture absorbed by the IC-package [automotive applications]," in *Proc. IEEE SENSORS*, Vienna, Austria, Oct. 2004, pp. 455–458.

[53] J. M. Cesaretti, W. P. Taylor, G. Monreal, and O. Brand, "Effect of stress due to plastic package moisture absorption in Hall sensors," *IEEE Trans. Magn.*, vol. 45, no. 10, pp. 4482–4485, Oct. 2009.

[54] M. Motz, U. Ausserlechner, and M. Holliber, "Compensation of mechanical stress-induced drift of bandgap references with on-chip stress sensor," *IEEE Sensors J.*, vol. 15, no. 9, pp. 5115–5121, Sep. 2015.

[55] M. Cornils and O. Paul, "Reverse-magnetic-field reciprocity in conductive samples with extended contacts," *J. Appl. Phys.*, vol. 104, no. 2, Jul. 2008, Art. no. 024505, doi: 10.1063/1.2951895.

[56] O. Paul and M. Cornils, "Explicit connection between sample geometry and Hall response," *Appl. Phys. Lett.*, vol. 95, no. 23 Art. no. 232112.

[57] G. Boero, M. Demierre, P.-A. Besse, and R. Popovic, "Micro-Hall devices: Performance, technologies and applications," *Sens. Actuators A, Phys.*, vol. 106, pp. 314–320, Sep. 2003. [Online]. Available: https://linkinghub.elsevier.com/retrieve/pii/S0924424703001924

[58] P. Munter, "A low-offset spinning-current Hall plate," *Sens. Actuators A, Phys.*, vol. 22, pp. 743–746, Jun. 1989. [Online]. Available: https://www.sciencedirect.com/science/article/pii/092442478980069X

[59] R. Steiner, C. Maier, M. Mayer, S. Bellekom, and H. Baltes, "Influence of mechanical stress on the offset voltage of Hall devices operated with spinning current method," *J. Microelectromech. Syst.*, vol. 8, no. 4, pp. 466–472, Dec. 1999. [Online]. Available: http://ieeexplore.ieee.org/document/809062/

[60] R. Steiner, A. Haberli, F.-P. Steiner, and H. Baltes, "Offset reduction in Hall devices by continuous spinning current method," in *Proc. Int. Solid State Sens. Actuators Conf. (Transducers)*, vol. 1, Jun. 1997, pp. 381–384.

[61] S. Bellekom, "CMOS versus bipolar Hall plates regarding offset correction," *Sens. Actuators A, Phys.*, vol. 76, nos. 1–3, pp. 178–182, Aug. 1999. [Online]. Available: https://linkinghub.elsevier.com/retrieve/pii/S0924424799000072

[62] S. Huber, W. Leten, M. Ackermann, C. Schott, and O. Paul, "A fully integrated analog compensation for the piezo-Hall effect in a CMOS single-chip Hall sensor microsystem," *IEEE Sensors J.*, vol. 15, no. 5, pp. 2924–2933, May 2015, doi: 10.1109/JSEN.2014.2385879.

[63] A. Ajbl, M. Pastre, and M. Kayal, "A fully integrated Hall sensor microsystem for contactless current measurement," *IEEE Sensors J.*, vol. 13, no. 6, pp. 2271–2278, Jun. 2013.

[64] S. Huber, Z. Lazar, M. Berger, and O. Paul, "A CMOS Hall-based magnetic multisensor system free from parasitic effects of temperature and package stress," in *Proc. 20th Int. Conf. Solid-State Sens., Actuators Microsyst. Eurosensors XXXIII (TRANSDUCERS EUROSENSORS XXXIII)*, Jun. 2019, pp. 134–137.

[65] M. Motz, U. Ausserlechner, W. Scherr, and B. Schaffer, "An integrated magnetic sensor with two continuous-time ΔΣ-converters and stress compensation capability," in *IEEE Int. Solid-State Circuits Conf. (ISSCC) Dig. Tech. Papers*, Feb. 2006, pp. 1151–1160.

[66] N. Kazemi, M. Abdolrazzaghi, P. Musilek, and M. Daneshmand, "A temperature-compensated high-resolution microwave sensor using artificial neural Network," *IEEE Microw. Wireless Compon. Lett.*, vol. 30, no. 9, pp. 919–922, Sep. 2020.

[67] N. Kazemi, M. Abdolrazzaghi, and P. Musilek, "Comparative analysis of machine learning techniques for temperature compensation in microwave sensors," *IEEE Trans. Microw. Theory Techn.*, vol. 69, no. 9, pp. 4223–4236, Sep. 2021.

[68] Z. Nenova and G. Dimchev, "Compensation of the impact of disturbing factors on gas sensor characteristics," *Acta Polytech. Hung*, vol. 10, no. 3, pp. 97–111, Jan. 2013.

[69] P. Khatri, K. K. Gupta, and R. K. Gupta, "Drift compensation of commercial water quality sensors using machine learning to extend the calibration lifetime," *J. Ambient Intell. Humanized Comput.*, vol. 12, no. 2, pp. 3091–3099, Feb. 2021, doi: 10.1007/s12652-020-02469-y.

[70] J. M. Margarit-Taulé, M. Martín-Ezquerra, R. Escudé-Pujol, C. Jiménez-Jorquera, and S.-C. Liu, "Cross-compensation of FET sensor drift and matrix effects in the industrial continuous monitoring of ion concentrations," *Sens. Actuators B, Chem.*, vol. 353, Feb. 2022, Art. no. 131123.

[71] M. Abdolrazzaghi, M. H. Zarifi, W. Pedrycz, and M. Daneshmand, "Robust ultra-high resolution microwave planar sensor using fuzzy neural network approach," *IEEE Sensors J.*, vol. 17, no. 2, pp. 323–332, Jan. 2017.

[72] N. Zimmerman et al., "A machine learning calibration model using random forests to improve sensor performance for lower-cost air quality monitoring," *Atmos. Meas. Techn.*, vol. 11, no. 1, pp. 291–313, 2018. [Online]. Available: https://amt.copernicus.org/articles/11/291/2018/

[73] P. Nowack, L. Konstantinovskiy, H. Gardiner, and J. Cant, "Machine learning calibration of low-cost NO_2 and PM_{10} sensors: Non-linear algorithms and their impact on site transferability," *Atmos. Meas. Techn.*, vol. 14, no. 8, pp. 5637–5655, 2021. [Online]. Available: https://amt.copernicus.org/articles/14/5637/2021/

[74] F. M. Heckmeier and C. Breitsamter, "Aerodynamic probe calibration using Gaussian process regression," *Meas. Sci. Technol.*, vol. 31, no. 12, Oct. 2020, Art. no. 125301, doi: 10.1088/1361-6501/aba37d.

[75] S. Urban, M. Ludersdorfer, and P. van der Smagt, "Sensor calibration and hysteresis compensation with heteroscedastic Gaussian processes," *IEEE Sensors J.*, vol. 15, no. 11, pp. 6498–6506, Nov. 2015.

[76] G. Tancev and F. G. Toro, "Variational Bayesian calibration of low-cost gas sensor systems in air quality monitoring," *Meas., Sensors*, vol. 19, Feb. 2022, Art. no. 100365. [Online]. Available: https://www.sciencedirect.com/science/article/pii/S2665917421003287

[77] C. M. Bishop, *Pattern Recognition and Machine Learning*, 6th ed. New York, NY, USA: Springer, 2006.

[78] C. E. Rasmussen and C. K. I. Williams, *Gaussian Processes for Machine Learning* (Adaptive Computation and Machine Learning). Cambridge, MA, USA: MIT Press, 2006.

[79] I. Goodfellow, Y. Bengio, and A. Courville, *Deep Learning*. Cambridge, MA, USA: MIT Press, 2016, http://www.deeplearningbook.org.

[80] M. Berger, S. Huber, C. Schott, and O. Paul, "Half-blind calibration for the efficient compensation of parasitic cross-sensitivities in nonlinear multisensor systems," *IEEE Sensors J.*, vol. 19, no. 16, pp. 7005–7014, Aug. 2019.

[81] A. Albert, *Regression and the Moore–Penrose Pseudoinverse*. New York, NY, USA: Academic, 1972.

[82] A. C. Atkinson, *Optimal Design*. Hoboken, NJ, USA: Wiley, 2015, pp. 1–17, doi: 10.1002/9781118445112.stat04090.pub2.

[83] B. Smucker, M. Krzywinski, and N. Altman, "Optimal experimental design," *Nature Methods*, vol. 15, no. 8, pp. 559–560, Jul. 2018, doi: 10.1038/s41592-018-0083-2.

[84] J. Lever, M. Krzywinski, and N. Altman, "Points of significance: Model selection and overfitting," *Nature Methods*, vol. 13, no. 9, pp. 703–704, 2016.

[85] M. Krzywinski and N. Altman, "Multiple linear regression," *Nature Methods*, vol. 12, no. 12, pp. 1103–1104, 2015.

[86] J. Lever, M. Krzywinski, and N. Altman, "Points of significance: Regularization," *Nature Methods*, vol. 13, no. 10, pp. 803–804, 2016, doi: 10.1038/nmeth.4014.

[87] M. Berger, F. Becker, and O. Paul, "Guidelines for multisensor system calibration with and without regularization," in *Proc. 20th Int. Conf. Solid-State Sens., Actuators Microsyst. Eurosensors XXXIII (TRANSDUCERS EUROSENSORS XXXIII)*, Jun. 2019, pp. 2103–2106.

[88] A. Gelman, J. B. Carlin, H. S. Stern, and D. B. Rubin, *Bayesian Data Analysis*, 3rd ed. New York, NY, USA: CRC Press, 2013.

[89] P. Virtanen et al., "SciPy 1.0: Fundamental algorithms for scientific computing in Python," *Nature Methods*, vol. 17, pp. 261–272, Feb. 2020.

[90] J. Wang, "Electrochemical glucose biosensors," *Chem. Rev.*, vol. 108, no. 2, pp. 814–825, Dec. 2007.

[91] A. Weltin, J. Kieninger, and G. A. Urban, "Microfabricated, amperometric, enzyme-based biosensors for in vivo applications," *Anal. Bioanal. Chem.*, vol. 408, no. 17, pp. 4503–4521, Jul. 2016.

[92] E. Foxlin and L. Naimark, "Miniaturization, calibration & accuracy evaluation of a hybrid self-tracker," in *Proc. 2nd IEEE ACM Int. Symp. Mixed Augmented Reality*, Tokyo, Japan, 2003, pp. 151–160. [Online]. Available: http://ieeexplore.ieee.org/document/1240698/

[93] Q. Yu and X. Zhou, "Pressure sensor based on the fiber-optic extrinsic Fabry–Pérot interferometer," *Photonic Sensors*, vol. 1, no. 1, pp. 72–83, Mar. 2011, doi: 10.1007/s13320-010-0017-9.

[94] V. Cimini et al., "Calibration of multiparameter sensors via machine learning at the single-photon level," *Phys. Rev. A, Gen. Phys.*, vol. 15, Apr. 2021, Art. no. 044003, doi: 10.1103/PhysRevApplied.15.044003.

[95] A. P. Singh, S. Kumar, and T. S. Kamal, "Virtual compensator for correcting the disturbing variable effect in transducers," *Sens. Actuators A, Phys.*, vol. 116, no. 1, pp. 1–9, Oct. 2004. [Online]. Available: https://www.sciencedirect.com/science/article/pii/S0924424704001955

Moritz Berger (Member, IEEE) received the M.Sc. degree in microsystems engineering from the Department of Microsystems Engineering (IMTEK), University of Freiburg, Germany, in 2017, where he is currently pursuing the Ph.D. degree in collaboration with Melexis Technologies SA, Bevaix, Switzerland.

In 2015, he gained practical experience as a Research and Development Intern at Silicon Microstructures, Milpitas, CA, USA, on pressure sensors. His MEMS-related research interests have been in new methods for the calibration of multisensor systems.

Mr. Berger was awarded the Third Prize of the International Contest on Applications of Nano-Micro Technologies (iCan) at Transducers 2015 in Anchorage, AK, USA, with a team of students of the University of Freiburg.

Christian Schott (Member, IEEE) received the M.Sc. degree in electrical engineering from the Technical University of Karlsruhe, Germany, in 1992, and the Ph.D. degree in magnetic sensors from the École polytechnique fédérale de Lausanne (EPFL), Lausanne, Switzerland, in 1999.

After the successful development of integrated Hall sensors with magnetic concentrators at Sentron AG, Zug, Switzerland, he joined Melexis Technologies SA, Bevaix, Switzerland, in 2004, contributing to make the triaxis technology a global success. Following different technical and management positions, he founded the Melexis Global Intellectual Property Team in 2013 and successfully led it through various court litigations and license negotiations. Since 2018, he has been working as a Process and Test Architect and preparing the future of magnetic testing at Melexis Technologies SA. He holds over 30 patents and has published over 40 articles.

Oliver Paul (Senior Member, IEEE) received the Diploma degree in physics and the D.Sc. degree from ETH Zürich, Switzerland, in 1986 and 1990, respectively.

After postdoctoral work at the Fraunhofer Institute for Solar Energy Systems, Freiburg, Germany, he joined the Physical Electronics Laboratory, ETH Zürich, as a Lecturer and a Group Leader in 1992. Since 1998, he has been a Full Professor with the University of Freiburg, Germany, where he heads the Laboratory for Microsystem Materials, Department of Microsystems Engineering (IMTEK), Faculty of Engineering. He is the Co-Founder of Sensirion AG, Stäfa, Switzerland, and Atlas Neuroengineering, Leuven, Belgium. He was the Director of IMTEK and the Dean of the Faculty of Engineering, University of Freiburg, from 2006 to 2008 and from 2016 to 2018, respectively. He was the Founding Director of the German Cluster of Excellence BrainLinks-BrainTools, University of Freiburg. He holds various advisory positions at the University of Freiburg. He is a coauthor of more than 400 technical publications, patents, and books. The research of his group focuses on MEMS materials and fabrication technologies, physical microtransducers, and microstructures for industrial and life science applications.

Dr. Paul has been a member of the Editorial Board of *Sensors and Actuators A: Physical* and *Journal of Micromechanics and Microengineering* and the Editorial Advisory Board of the *IEEJ Transactions on Electrical and Electronic Engineering*. He co-chaired the IEEE MEMS 2004 Conference.